Design of metallic nanoparticle gratings for filtering properties in the visible spectrum

Y. Brûlé,[1] G. Demésy,[1] A.-L. Fehrembach,[1] B. Gralak,[1,*] E. Popov,[1] G. Tayeb,[1]
M. Grangier,[2,3] D. Barat,[3] H. Bertin,[2] P. Gogol,[2] and B. Dagens[2]

[1]CNRS, Aix-Marseille Université, Centrale Marseille, Institut Fresnel UMR 7249, 13013 Marseille, France
[2]IEF, CNRS, Université Paris-Sud, Université Paris-Saclay, 91405 Orsay, France
[3]PSA Peugeot Citroën, Direction Scientifique, Centre Technique de Vélizy, Route de Gisy, Vélizy-Villacoublay F-78140, France
*Corresponding author: boris.gralak@fresnel.fr

Plasmonic resonances in metallic nanoparticles are exploited to create efficient optical filtering functions. A finite element method is used to model metallic nanoparticle gratings. The accuracy of this method is shown by comparing numerical results with measurements on a two-dimensional grating of gold nanocylinders with an elliptic cross section. A parametric analysis is then performed in order to design efficient filters with polarization dependent properties together with high transparency over the visible range. The behavior of nanoparticle gratings is also modeled using the Maxwell–Garnett homogenization theory and analyzed by comparison with the diffraction of a single nanoparticle. The proposed structures are intended to be included in optical systems that could find innovative applications.   © 2015 Optical Society of America

OCIS codes: (230.7408) Wavelength filtering devices; (050.5745) Resonance domain; (050.1755) Computational electromagnetic methods; (220.4241) Nanostructure fabrication.

http://dx.doi.org/10.1364/AO.54.010359

1. INTRODUCTION

Metallic nanoparticles supporting plasmonic resonances can be used to design optical functions, for instance, filtering properties, or chemical and bio-sensing [1,2]. Such systems offer several advantages such as the possibility of controlling the operating wavelength with the nature of the metal, the size of the particles, the polarization of the illumination, etc. In this paper, we focus on the design of a spectral filtering property in reflectivity, i.e., the frequency selective mirror property. In particular, challenges lie in obtaining a narrow reflection peak while keeping absorption losses as low as possible and a transmission level averaged over the visible range as high as possible.

Reflective color filters based on plasmonic resonators have already been proposed in the literature. In [3], different arrays of metallic nanodisks are deposited on a backreflector made of silver and gold to print a color image at the optical diffraction limit. Dense silver nanorod arrays are used in [4] to create reflective color filters at specific wavelengths depending on the arrays' geometry. Nevertheless, in these propositions, the overall transmission remains low. Core–shell nanoparticles, made of silica and silver and embedded into a polymer matrix, were proposed in [5] to make transparent displays based on resonant nanoparticle scattering. The considered filters have reflection properties at defined wavelengths and global transparency over

the visible spectrum. However, the latter structure, based on the scattering phenomenon, does not work as a mirror, but as a display with a virtual image located in the reflecting structure. High resolution color transmission filtering and spectral imaging have also been achieved [6] where plasmonic nanoresonators, formed by subwavelength metal–insulator–metal stack arrays, allow efficient manipulation of light and control of the transmission spectra. Also, highly transmissive plasmonic subtractive color filters are proposed in [7] with a single optically thick nanostructured metal layer thanks to the counterintuitive phenomenon of extraordinary transmission.

In this paper, the main objective is to design metallic nanoparticle gratings in order to obtain a filtering property for wavelengths in the visible range with relatively low absorption. First, we present the formulation of the finite element method (FEM) [8] chosen to model the considered structures and whose accuracy has been checked by comparing it with the Fourier modal method [9]. The relevance of this numerical tool is shown by comparing full three-dimensional numerical calculations with measurements on fabricated samples. The numerical tool is then exploited to perform a parametric analysis of the influence of geometric parameters and polarization on filtering properties and absorption. Next, this parametric analysis is used to propose optimized filtering systems with a high level
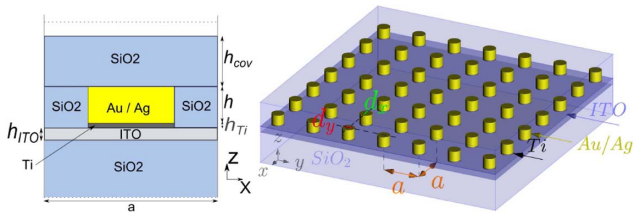
Fig. 1.   Schemes of the considered nanoparticle gratings.

Fig. 2.   Scheme of the illumination conditions for wave vector $\boldsymbol{k}^+$ lying in the xz plane ($\psi_0 = 0$).

of transparency on average in the visible spectrum. In addition, different models are proposed to analyze the behavior of the nanoparticle gratings. An analytical homogenization model based on the Maxwell–Garnett approximation is faced to the rigorous FEM calculations. Finally, the multipolar radiation of a single nanoparticle is compared to the diffractive properties of a grating consisting of the same nanoparticles.

The considered gratings are defined as two-dimensional square arrays of metallic nanoparticles on a glass (SiO$_2$) substrate. The lattice constant of the array along the two directions x and y is denoted by a. On each node of this array lies a gold (Au) or silver (Ag) nanocylinder with an elliptic cross section of height h and diameters d_x and d_y (along the x and y directions, respectively). Note that for fabrication requirements an optional indium tin oxide (ITO) thin film layer of height h_{ITO} may be added on top of the substrate, and a second optional attaching layer of titanium (Ti) of height h_{Ti} may also be added to the bottom of the nanocylinder. Finally, a nanocylinder grating can be embedded into a SiO$_2$ cover layer of height h_{cov} from the top of the nanocylinder. Figure 1 presents schemes of the considered structures. Finally, the refractive indices of the different materials for the simulations are taken from [10] for SiO$_2$, [11] for gold, [12] for silver, and [13] for Ti.

2. NUMERICAL MODELING

A. Finite Element Method Formulation

The FEM formulation used in this paper is described in [8]. This numerical method allows calculation in the time-harmonic regime of the vector fields diffracted by any arbitrarily shaped crossed grating embedded in a multilayered stack. The considered grating (Fig. 1) is placed in an air superstrate (incident) medium with permittivity $\epsilon^+ = 1$. The SiO$_2$ substrate is considered semi-infinite with permittivity ϵ^-. All materials of the structure are considered nonmagnetic ($\mu_r = 1$). The time-harmonic regime with a $\exp[-i\omega t]$ dependence is considered where the frequency ω is related to a wavelength $\lambda = 2\pi c/\omega$ in vacuum and c is the speed of light in vacuum. The grating is illuminated with a plane wave $\boldsymbol{E}_0 = A_0 \exp[i\boldsymbol{k}^+ \cdot \boldsymbol{x}]$, where the wave vector $\boldsymbol{k}^+$ is defined by $\|\boldsymbol{k}^+\| = k^+ = k_0 = \omega/c$ and the two angles $\theta_0 \in [0, \pi/2]$ and $\psi_0 \in [0, 2\pi]$ ($\boldsymbol{k}^+$ is in the xz plane if $\psi_0 = 0$ and $\boldsymbol{k}^+$ is in the yz plane if $\psi_0 = \pi/2$). This incident plane wave is p-polarized if the electric field is inside the incident plane (see left panel of Fig. 2) and s-polarized if the electric field is perpendicular to the incident plane (see right panel of Fig. 2).
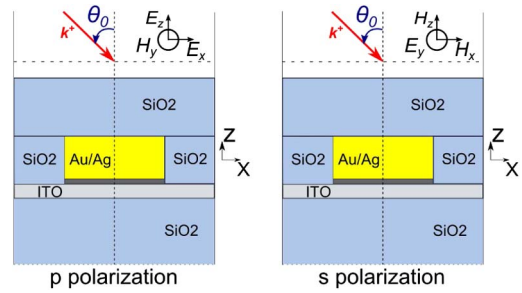
We want to retrieve the total electromagnetic field $(\boldsymbol{E}, \boldsymbol{H})$ solution of the Helmholtz equation

$$\nabla \times \nabla \times \boldsymbol{E} + k_0^2 \mu_0 \epsilon \boldsymbol{E} = 0, \tag{1}$$

where the diffracted field defined as $\boldsymbol{E}_d = \boldsymbol{E} - \boldsymbol{E}_0$ satisfies an outgoing wave condition and where the field $\boldsymbol{E}$ is quasi-periodic along the two directions x and y. The vector field $\boldsymbol{E}_d$ diffracted by the structure is calculated using the solution of an ancillary problem that corresponds to the associated multilayered diffraction problem (that is, without any diffractive element and with the same condition of illumination). This intermediate solution is then used as a known vectorial source term whose support is localized inside the diffractive element itself. Hence, the total field $\boldsymbol{E}$ of the structure is compound of three fields: (i) the diffracted field $\boldsymbol{E}_d$ calculated using the FEM; (ii) the incident plane wave $\boldsymbol{E}_0$; and (iii) the plane waves diffracted by the multilayer structure (the diffracted field associated with the ancillary problem that is compound of the transmitted and reflected waves of the multilayer structure). Because the total field $\boldsymbol{E}$ has Bloch-boundary conditions along the two directions of periodicity, the computation domain is then reduced to a single cell of the grating through the set $(k_x, k_y) \equiv (k_x^+, k_y^+)$ imposed by the incident plane wave. [Note that the whole structure of the two-component wave vector (k_x, k_y) has the same grating periodicity; hence (k_x^+, k_y^+) is denoted by (k_x, k_y).] The implementation of those specific boundary conditions adapted to the FEM is described in [14]. As mentioned above, the diffracted field $\boldsymbol{E}_d$ should also satisfy an outgoing wave condition in the z direction. Thus, a set of perfectly matched layers (PML [15]) is introduced to truncate the substrate and superstrate along the z axis. Indeed, the diffracted field that radiates from the structure toward the infinite regions decays exponentially inside the implemented PML along the z axis.

Once the values of the fields in the whole structure are obtained, they are used to compute a complete energy balance of the bi-periodic grating. It is based on (i) the calculation of the diffraction efficiencies of each reflected and transmitted order along the gratings' two directions of periodicity through a double Rayleigh expansion of the fields and (ii) the calculation of the normalized losses of each part of the diffractive (absorptive) element of the cell. This energy balance is then used to check the accuracy and self-consistency of the whole calculation because the sum of the different components of the energy balance should be equal to 1.

The described method has been implemented into the following free FEM software: Gmsh [16], a mesh generator and visualization tool, and GetDP [17], a finite element library. Numerous comparisons with the Fourier modal method [9] have been performed to check the accuracy of the present FEM method.

B. Comparison with Measurements

Samples have been fabricated in order to check the relevance of the numerical tool. We use a commercial SiO_2 substrate covered by a 40 nm ITO layer. This ITO layer is used to evacuate charges during the lithography process. On this ITO thin film, a 4 nm Ti adhesion layer and a 30 nm gold film were deposited by electron beam evaporation. The gold nanocylinders are then realized by electron beam lithography. Scanning electron microscopy (SEM) imaging of the realized gratings are then performed that allow measurements of dimensions of the realized elliptical nanocylinders. Three gold nanocylinder gratings with different square periodicities have been fabricated: S1 ($a = 200$ nm), S2 ($a = 250$ nm), and S3 ($a = 300$ nm). The elliptical diameters d_x and d_y of the nanocylinders for the three fabricated structures S1–S2–S3 are approximately 80 and 120 nm, respectively (see Table 1 for the exact dimensions). Figure 3 shows a scheme and a SEM image of one of these gratings.

The optical characterization of the samples is based on the transmission measurement. A polychromatic source (Xe lamp) illuminates the samples through a monochromator and a polarizer. The source illuminating the samples is then almost monochromatic (400–1100 nm wavelength) and is linearly polarized. The transmission measurement is then performed with a homemade angulo-spectral optical reflectivity and transmissivity bench. Notice that this transmission measurement is normalized with respect to transmission for the bare SiO_2 substrate.

Transmission measurements were performed for an incident beam in normal incidence with an electric field polarized along the y direction (s polarization) and the x direction (p polarization) for wavelengths ranging from 500 to 1100 nm. These

Table 1.   Cylinder Dimensions of the Three Fabricated Structures

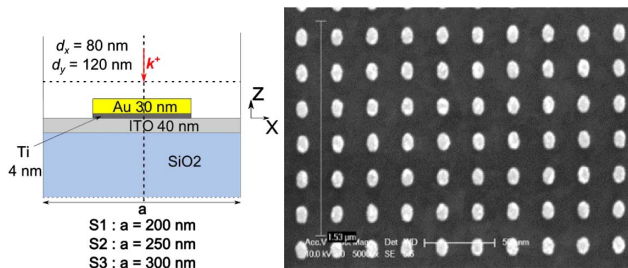|	a (nm)	d_x (nm)	d_y (nm)
S1	200	91	129
S2	250	87	125
S3	300	84	122

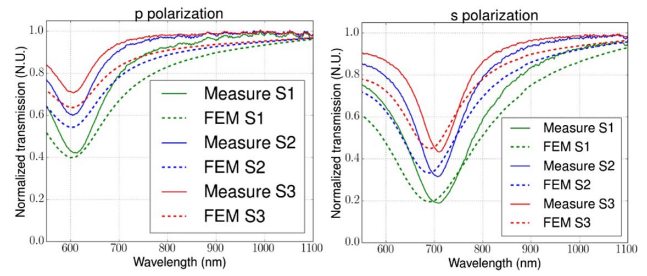**Fig. 3.**   Scheme and SEM imaging of the fabricated structures S1–S2–S3.

Fig. 4.   Comparison between the FEM results (dashed) and the measurements (solid) in transmission for the three fabricated samples S1–S2–S3.

measurements are compared with the simulation results, where the gratings' transmission efficiencies have been also normalized by the transmission of the bare SiO_2 substrate. Notice that the Au refractive index considered in these simulations for comparison is determined from measurements on the samples (there is a small difference from data in [11]). Figure 4 shows excellent qualitative and quantitative agreement and thus the relevance of the numerical tool employed to design plasmonic filters. The small remaining differences between the measurements and calculations can be attributed to the deviations in the shape of the fabricated cylinders, for example, slanted walls or rounded corners.

3. PARAMETRIC ANALYSIS AND DESIGN OF FILTERING PROPERTIES

In this section, the influence of the different system parameters (nature of the metal, geometric parameters, and illumination polarization) is analyzed in the case of an illumination with oblique incidence ($\theta_0 = 45°$). This analysis is used to design an optimized structure for filtering properties. Here, the challenges are to obtain a choice of resonances in the visible spectrum with a minimum of optical losses or a maximum of averaged transmission.

From results presented in the previous section, it appears that structures of Au nanocylinders lead to resonances of around 700 nm. Hence, Ag nanocylinders are considered in Subsection 3.A to address the whole visible spectrum for reflectivity peaks. Next, in Subsection 3.B, the presence of absorption is analyzed starting from the reference structures S1–S2–S3 of Au nanoparticles. Finally, in Subsection 3.C, optimized structures are proposed.

A. Influence of Cylinder Diameters and Incident Polarization on the Resonance Wavelength

The geometries considered in this subsection are similar to the ones of Subsection 2.B (see Fig. 5) with the same ITO and Ti layers. The differences are: a 300 nm SiO_2 cover layer in order to prevent the oxidation of the Ag nanocylinders; square periodicity of the gratings fixed to $a = 200$ nm; Ag elliptical nanocylinders with axes d_x fixed to 100 nm and d_y varying from 100 to 180 nm with a 20 nm pitch (type S4 structures). Here, Ag nanocylinders have been introduced in order to address the whole visible spectrum with plasmonic resonances.
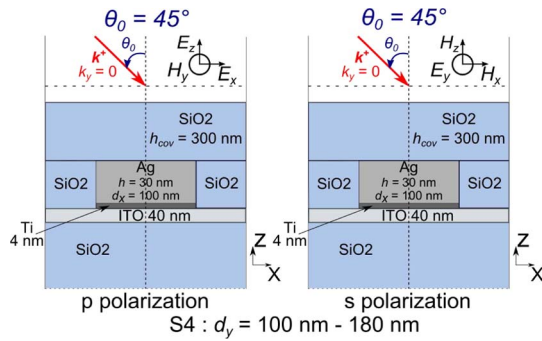
Fig. 5. Scheme of the structure S4 for the considered conditions of illumination.

Simulations are performed for a plane wave with a wave vector lying in the xz plane ($k_y = 0$), where the angle of incidence with respect to the normal of the substrate is $\theta_0 = 45°$. Both polarizations are considered (see Fig. 5). Simulations are performed for wavelengths spanning the visible range (380 to 780 nm). Figure 6 shows the transmission efficiency in the specular order for the various d_y diameters, for p and s polarizations. The corresponding efficiencies in the reflection specular order are reported in Fig. 7. In the present case of an incident plane wave with a wave vector lying in the xz plane ($k_y = 0$), the electric field "sees" the small axis d_x of the elliptical nanocylinder when the plane wave is s-polarized. However, when the plane wave is s-polarized, the electric field "sees" the large axis d_y. One can observe in Figs. 6 and 7 that the resonance occurring for p polarization is at a lower wavelength and is less efficient than the one that occurs for s polarization. The more the incident electric field meets a high
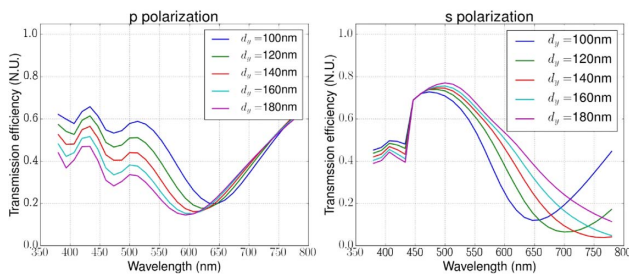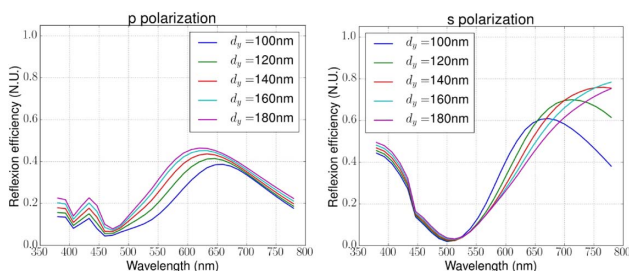
quantity of metal, the more the resonance is pronounced and redshifted. Also, in the two cases of polarization, increasing d_y broadens the reflection peaks, which is consistent with an increasing quantity of metal. While increasing d_y, one can observe that the reflection peak in p polarization is blueshifted, while the one in s polarization is redshifted. Hence the two resonances in the two polarizations are not totally independent, but the general tendencies described above remain valid. These effects may allow us to manipulate the resonances observed in those elliptical nanocylinder gratings and to select wavelengths for which the reflection peaks depend on the incidence plane of the waves and their polarization. Hence, the first challenge to obtain a resonance at the desired wavelength in the whole visible spectrum might be addressed.

B. Absorption and Influence of Geometrical Parameters

The second challenge is to reduce absorption in order to obtain a high transmission when averaged on the whole visible spectrum. The influence of the quantity of metal is thus investigated in detail.

As a preliminary, we observe that, from the simulated total energy balance obtained for structure S2 (see Fig. 8), losses are important inside the ITO and Ti layers. Since these materials play no role in the filtering function, suppressing ITO and Ti layers should be addressed in order to reduce Joule losses. The investigation is now performed with gold nanocylinder gratings directly deposited on the SiO$_2$ substrate.

The influence of the quantity of metal is investigated by increasing the filling fraction of metal using two groups of structures. For the first group of structures S5 (left panel of Fig. 9), the size of the nanocylinders is increased for a fixed lattice constant a. Conversely, for the second group of structures S6 (right panel of Fig. 9), the size of the lattice constant a is increased for a fixed nanocylinder dimension. Also, to simplify the number of parameters of influence, nanocylinders with circular cross sections are considered here. The plane wave illuminating the structures has a wave vector lying in the xz plane ($k_y = 0$) with an angle of incidence fixed to $\theta_0 = 45°$ and is s polarized.

First, the influence of the nanocylinder's diameter on the total energy balance spectrum is analyzed. Notice that the propagative diffraction efficiencies higher than the (0, 0) specular orders are omitted since they are found to be negligible. The square pitch of the grating is fixed with $a = 250$ nm; the gold nanocylinder height is fixed to $h = 30$ nm; and the group of

Fig. 6. Efficiency in the transmission specular order for the S4 group of structures.

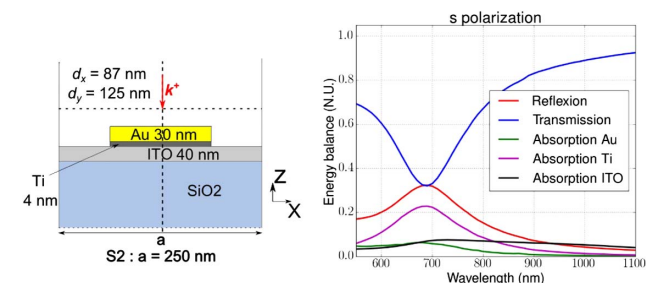**Fig. 7.** Efficiency in the reflection specular order for the S4 group of structures.

Fig. 8. Decomposition of the total energy balance for s polarization for the structure S2.
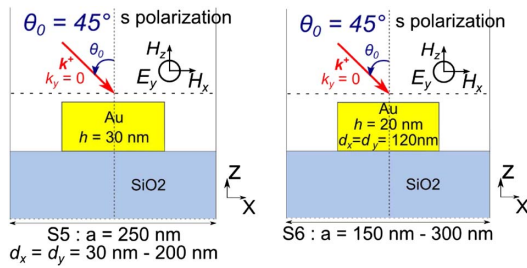
Fig. 9.   Scheme of the structures S5 (left panel) and S6 (right panel).

structures S5 have diameters that vary from 30 to 200 nm with 10 nm pitch. The left panel of Fig. 10 shows the reflection efficiency in the specular order in the visible range (380 to 780 nm) as a function of the nanocylinder's diameter. One can observe that as the nanocylinder's diameter increases, the reflection peak intensity is magnified, redshifted, and broadened. Again, one can possibly choose the operating wavelength of the filter by selecting the appropriate diameter.

Second, the influence of the lattice constant a on the total energy balance spectrum is analyzed. The nanocylinder's geometry is then fixed with a height $h = 20$ nm and a diameter $d_x = d_y = 120$ nm. The square periodicity a is now spanning the range (150 to 300 nm) with a 25 nm pitch (group of structures S6). The illumination configuration remains unchanged (incident angle of 45°, $k_y = 0$, and s polarization). The right panel of Fig. 10 presents the spectrum of the reflection efficiency in the specular order over the visible range (380–780 nm) as a function of the lattice constant a. For fixed nanocylinder dimensions, increasing the grating square periodicity leads to slight variations of the central wavelength of the reflectivity peaks, which confirms that resonance frequency is mainly governed by particle diameter. Moreover, the intensity decreases, and the peak is sharpened with the increase of the grating's periodicity. This result is fully consistent with the study on the influence of diameter.

Combining these two parametric investigations leads to four conclusions: (i) the resonance frequency is mainly governed by nanocylinder dimensions; (ii) the ratio of the nanocylinder's cross section surface over the lattice unit cell surface a^2 mainly governs the resonance intensity and absorption; and conclusions (iii) and (iv) are noted in the next paragraph.

Before presenting optimized structures, it is stressed that, in the configurations S5 and S6, efficient reflectivity peaks occur
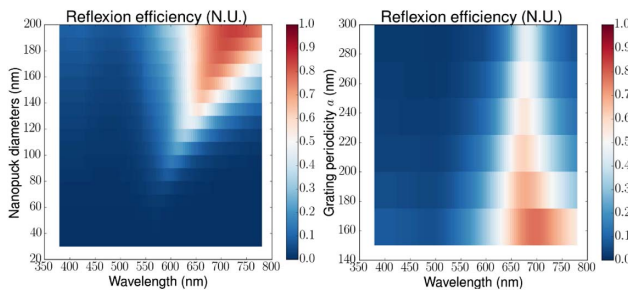
for wavelengths around 650 nm. If the structure is embedded into SiO₂ (e.g., structures S2 in Section 2), then the observed peak in reflection is redshifted and will occur only in the extreme red part of the visible spectrum around 700 nm (for structures S2). Thus, as conclusion (iii), it appears necessary to consider the solution based on Ag proposed in Subsection 3.A to blueshift the resonances since the plasma frequency of Ag occurs at lower wavelengths. Finally, as pointed out at the beginning of this subsection, high absorption appears in ITO and Ti layers (Fig. 8), and thus optimization should be performed for nanocylinders standing directly on a SiO₂ substrate [conclusion (iv)].

C. Optimized Design with Silver Elliptical Nanocylinders

In this section, we propose two different designs of silver elliptical nanocylinder gratings embedded in SiO₂, leading to peaks in the specular reflectivity in the visible range. The elliptical cross section of the nanocylinders allows two different peaks at two different wavelengths for a unique structure, depending on the polarization of illumination. The proposed filters also possess properties of global transparency on the visible spectrum.

The first proposed filter F1 is comprised of nanocylinders of 30 nm height (left panel of Fig. 11). The ellipse's diameters are $d_x = 80$ nm and $d_y = 60$ nm. The grating is embedded into SiO₂; the substrate is SiO₂, and a SiO₂ cover layer of 200 nm is added. The square periodicity a of the grating is fixed to 200 nm. The incident wave vector lies either in the xz plane ($k_y = 0$) or in the yz plane ($k_x = 0$), with an angle of incidence fixed to $\theta_0 = 45°$, and both p and s polarizations are considered. Figure 12 shows the different components of the energy balance for the filtering structure F1. This geometry leads to reflection peaks in the specular order centered at two different wavelengths (525 and 590 nm) depending on the incidence plane and polarization.

The second proposed filter F2 is made of nanocylinders with 40 nm height (right panel of Fig. 11). Ellipse diameters are $d_x = 100$ nm and $d_y = 60$ nm. The grating is embedded into SiO₂ (cover layer of 200 nm and substrate). The square periodicity a of the grating remains 200 nm, and the illumination conditions are the same as those for F1. Figure 13 shows the different components of the energy balance for grating F2. Here, reflection peaks are obtained at the two different wavelengths, 520 and 633 nm. In both cases, the averaged transmission over the whole visible spectrum is above 64%, which
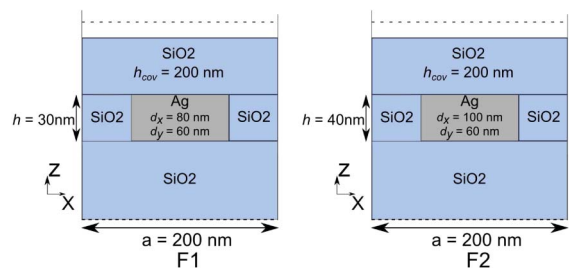

Fig. 10.   Left panel: Reflection efficiency in the specular order for structures S5. Right panel: Reflection efficiency in the specular order for structures S6.

Fig. 11.   Schemes of the optimized filters F1 (left panel) and F2 (right panel).
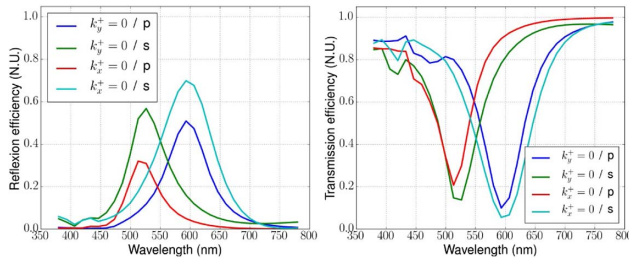
Fig. 12. Reflection (left panel) and transmission (right panel) efficiencies in the specular order for the structure F1.
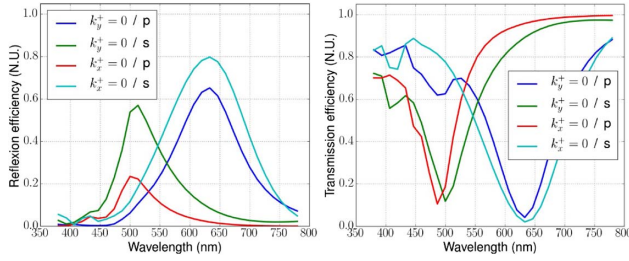

Fig. 13. Reflection (left panel) and transmission (right panel) efficiencies in the specular order for the structure F2.

ensures correct transparency. This is confirmed by the absorption spectra of the two structures shown in Fig. 14.

4. HOMOGENIZATION OF NANOCYLINDER STRUCTURES

In this section, the properties of nanoparticle gratings are modeled using Maxwell–Garnett homogenization. A detailed discussion of this homogenization of elliptic nanoparticles can be found in [18] and more recently in [19].

In the present case, we consider anisotropic inclusions for which the effective permittivity components $\epsilon_j (j = x, y, z)$ are given by

$$\epsilon_j - \epsilon_m = \epsilon_m \frac{f(\epsilon_p - \epsilon_m)}{\epsilon_m + L_j(\epsilon_p - \epsilon_m)} \left[1 - L_j \frac{f(\epsilon_p - \epsilon_m)}{\epsilon_m + L_j(\epsilon_p - \epsilon_m)}\right]^{-1}.$$

$$(2)$$

Here, ϵ_p and ϵ_m are the permittivity of the particles and the surrounding medium, respectively; f is the filling fraction of metal; and L_j are the components of the depolarization dyadic
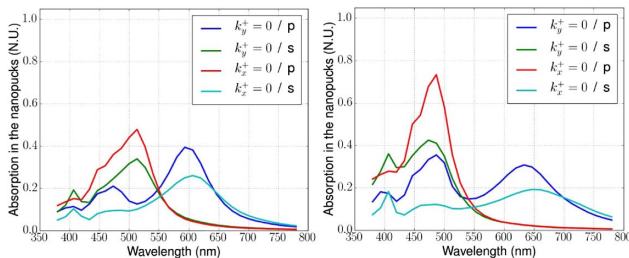

Fig. 14. Absorption in the nanocylinders for structures F1 (left panel) and F2 (right panel).
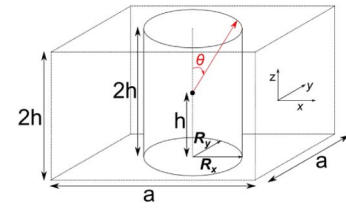

Fig. 15. Scheme of the considered unit cell.

in the corresponding axis ($j = x, y, z$). We consider a cylindrical inclusion of an elliptical cross section oriented in the z direction embedded into a rectangular box. The height of the rectangular box is equal to the height $2h$ of the cylinder (see Fig. 15). The basis of the rectangular box is the square unit cell of a lattice. Hence the filling fraction f is just the ratio of the cylinder section (an ellipse of radius $R_x = d_x/2$ and $R_y = d_y/2$) with respect to a^2, i.e., $f = \pi R_x R_y / a^2$.

The calculation of depolarization components is reported in Appendix A in both cases: cylinders with circular cross section (Appendix A.1) and elliptic cross section (Appendix A.2). After computing the different depolarization factors, the effective permittivity components are calculated from Eq. (2).

This effective model has been applied to a square unit cell ($a = 200$ nm) composed of a silver cylinder of elliptical cross section with radii $R_x = 40$ nm and $R_y = 30$ nm and height $2h = 30$ nm. The considered background medium is SiO$_2$. Hence, this unit cell represents the grating corresponding to structure F1. The following depolarization components are obtained using Eqs. (18) and (22): $L_x = 0.16$, $L_y = 0.24$, and $L_z = 0.60$. The corresponding effective anisotropic relative permittivity components are reported in the left panel of Fig. 16. One can check that the effective permittivity components show resonances around 480 and 575 nm. Next, the multilayer corresponding to structure F1 is considered. The multilayer is composed of (from top to bottom): (1) an incident medium (air); (2) a 200 nm SiO$_2$ layer corresponding to the cover layer; (3) a 30 nm homogenized layer of effective permittivity given in the left panel of Fig. 16 corresponding to the grating; and (4) a SiO$_2$ substrate. The reflection and transmission coefficients have been calculated for an incident plane wave with an incident wave vector that lies either in the xz plane ($k_y = 0$) or in the yz plane ($k_x = 0$) with an angle of incidence fixed to $\theta_0 = 45°$ and for wavelengths spanning the visible range. Both p and s polarizations have been considered and compared to the rigorous FEM calculation of Subsection 3.C. This comparison is shown in Fig. 17.
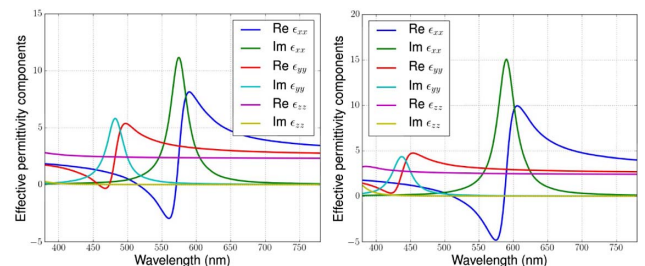

Fig. 16. Effective anisotropic relative permittivity components for the unit cell of structures F1 (left panel) and F2 (right panel).
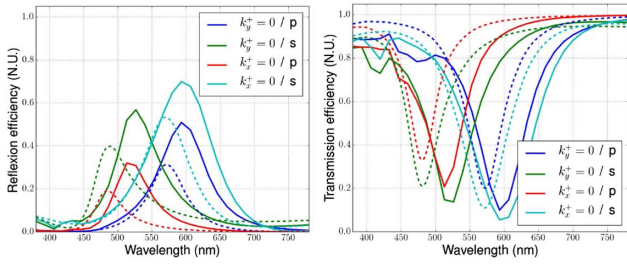
Fig. 17. Reflection (left panel) and transmission (right panel) efficiencies of structure F1 obtained with a rigorous FEM calculation (solid line) and homogenization model (dashed line).
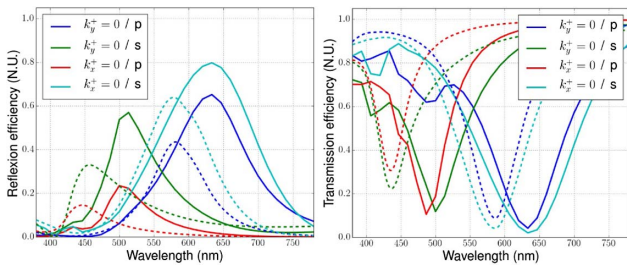

Fig. 18. Reflection (left panel) and transmission (right panel) efficiencies of structure F2 obtained with the rigorous FEM calculation (solid line) and homogenization model (dashed line).

The same reasoning has been applied to structure F2 and leads to the following depolarization components: $L_x = 0.16$, $L_y = 0.32$, and $L_z = 0.52$. The corresponding effective relative permittivity is plotted in the right panel of Fig. 16, and presents resonances of around 440 and 575 nm. The reflection and transmission coefficients for the effective multilayer are compared to FEM results in Fig. 18.

One can observe that the homogenization leads to resonances that are in relative agreement with the rigorous FEM results, except for a shift of about 50 nm for the resonance wavelength. This shift can be attributed to the effect of the finite size of the particles because it can be checked numerically that this shift decreases together with the particle size. These resonances are present in both the effective permittivity components and the spectra of transmission and reflection. Hence, these homogenization results provide useful tendencies with much faster computation time and can be used to design filtering properties.

Notice that a similar homogenization model can be derived in the more complex situation where the particles stand directly on a substrate without a cover layer (for instance, structures S5 or S6). For such a case, the calculation of the depolarization factors is given in Appendix A.3.

5. DIFFRACTION BY A SINGLE NANOCYCLINDER

In this last section, the contribution of the single nanoparticle to the electromagnetic behavior of the grating is analyzed. To that end, the problem of plane wave scattering by a single nanoparticle is solved numerically using the FEM via an approach similar to that in Subsection 2.A by changing Bloch–Floquet

boundary conditions to perfectly matched layers. Finally, a multipole expansion of the diffracted field is performed and discussed.

Consider a nonmagnetic scatterer of arbitrary shape with relative permittivity ε_s^b that is embedded in a transparent nonmagnetic homogeneous background of relative permittivity ε_r^b. We denote by $\varepsilon_r(\mathbf{x})$ the piecewise constant function equal to ε_s^b within the scatterer and ε_r^b elsewhere. The scatter is enlighten by a plane wave of arbitrary incidence and polarization $\boldsymbol{E}_0$. This incident field, i.e., the field without the scatterer, is the solution of the vector Helmholtz propagation equation in the resulting homogeneous medium

$$\nabla \times \nabla \times \boldsymbol{E}_0(\mathbf{x}) + k_0^2 \varepsilon_r^b \boldsymbol{E}_0(\mathbf{x}) = \mathbf{0}. \tag{3}$$

We are looking for the total field $\boldsymbol{E}$ resulting from the electromagnetic interaction of the scatterer and the incident field, which is the solution of the Helmholtz equation

$$\nabla \times \nabla \times \mathbf{E}(\mathbf{x}) + k_0^2 \varepsilon_r(\mathbf{x})\mathbf{E}(\mathbf{x}) = \mathbf{0}. \tag{4}$$

The field diffracted or scattered by the object is defined as $\boldsymbol{E}_d := \boldsymbol{E} - \boldsymbol{E}_0$. Combining Eqs. (3) and (4) allows us to reformulate the scattering problem as a radiation problem. The scattered field, now $\boldsymbol{E}_d$, satisfies the following propagation equation:

$$\nabla \times \nabla \times \boldsymbol{E}_d(\mathbf{x}) + k_0^2 \varepsilon_r(\mathbf{x})\boldsymbol{E}_d(\mathbf{x}) = k_0^2(\varepsilon_r(\mathbf{x}) - \varepsilon_r^b)\boldsymbol{E}_0(\mathbf{x}), \tag{5}$$

such that $\boldsymbol{E}_d$ satisfies a radiation condition. The right hand side can be viewed as a volume (current) source term with support of the scatterer itself, and $\varepsilon_r(\mathbf{x}) - \varepsilon_r^b$ is equal to $\varepsilon_s^b - \varepsilon_r^b$ inside the scatterer and 0 elsewhere.

The scattered field $\boldsymbol{E}_d$ can be expanded on the basis of outgoing vector partial waves $(\mathbf{M}_{n,m}^{(+)}, \mathbf{N}_{n,m}^{(+)})$ built upon the vector spherical harmonics $(\mathbf{X}_{n,m}, \mathbf{Y}_{n,m}, \mathbf{Z}_{n,m})$ following the framework and conventions described in detail in [20,21]

$$\mathbf{M}_{n,m}^{(+)}(k\mathbf{r}) = h_n^{(+)}(kr)\mathbf{X}_{n,m}(\theta, \varphi), \tag{6}$$

$$\mathbf{N}_{n,m}^{(+)}(k\mathbf{r}) = \frac{1}{kr}\left[\sqrt{n(n+1)}h_n^{(+)}(kr)\mathbf{Y}_{n,m}(\theta, \varphi)\right.$$
$$\left. + \xi'(kr)\mathbf{Z}_{n,m}(\theta, \varphi)\right]. \tag{7}$$

The so-called multipole expansion is finally given by

$$\boldsymbol{E}_d(\mathbf{r}) = \sum_{n=1}^{n_{\max}} \sum_{m=-n}^{m} f_{n,m}^{(h)}\mathbf{M}_{n,m}^{(+)}(k\mathbf{r}) + f_{n,m}^{(e)}\mathbf{N}_{n,m}^{(+)}(k\mathbf{r}), \tag{8}$$

where $f_{n,m}^{(h)}$ and $f_{n,m}^{(e)}$ can be numerically computed on any sphere of radius R englobing the scatterer

$$f_{n,m}^{(e)} = \frac{kR}{\xi'(kR)} \int_0^{2\pi} \int_0^{\pi} \boldsymbol{E}_d(R, \theta, \varphi) \cdot \mathbf{Z}_{n,m}^{\star}(\theta, \varphi) \mathrm{d}\theta \mathrm{d}\varphi, \tag{9}$$

$$f_{n,m}^{(h)} = \frac{kR}{h_n^{(+)}(kR)} \int_0^{2\pi} \int_0^{\pi} \boldsymbol{E}_d(R, \theta, \varphi) \cdot \mathbf{X}_{n,m}^{\star}(\theta, \varphi) \mathrm{d}\theta \mathrm{d}\varphi. \tag{10}$$

Note that $\boldsymbol{E}_d$ in Eqs. (9) and (10) is expressed from the FEM inherited Cartesian coordinates to spherical coordinates. This expansion is the classical way to obtain the far field radiation pattern of antennas. It would require major

adjustments to take into account the substrate and superstrate. First of all, let us state that the resonant phenomena described in the previous section do not depend on the close vicinity of the interface. Figure 19 shows the reflectivity of silver nanocylinder gratings of the optimized structure F1 when embedded in a homogeneous infinite SiO_2 background. In this simplified model, the θ_0 incidence is adjusted to compensate for the missing refraction at the SiO_2 interface $\theta_0 = \arcsin(\sin(45°)/n_{SiO_2}) \approx 29°$. The same four resonances as in Fig. 14 are obviously excited with $\theta = 29°$ depending on the plane of incidence (compare dashed and solid lines in Fig. 19). The only noticeable difference in the *s* polarization case (see green and cyan lines in Fig. 19) can be partly explained by the fact that at 45° incidence, reflection on a bare silica diopter is ~8.3% in *s* polarization, while only ~0.5% in *p* polarization, due to the Brewster effect).

Consider now the single scatterer case. First of all, the only non-negligible terms in the expansion given in Eq. (8) correspond to electric dipoles no matter what the considered incidence is. All higher electric orders and all magnetic orders are at least 50-fold lower in magnitude than the dipolar electric ones over the whole visible spectrum. As shown in Figs. 20(a) and 20(b) for $k_y = 0$, i.e., when the incidence plane contains the r_x-axis of the ellipse, two resonant scenarios occur depending on the incident polarization. With *p* polarization [Fig. 20(a)], the incident electric field lies within the plane of incidence, and two electric multipoles dominate the far field scattered power corresponding to induced electric dipoles of moments along Ox (see $f^{(e)}_{1,\pm1}$) and Oz (see $f^{(e)}_{1,0}$). Heuristically, the incident electric field only *sees* two characteristic dimensions of the scatterer, i.e., the height *h* of the elliptic nanocylinder and its greater diameter $2r_x$. With *s* polarization, the only induced dipole present is along Oy, corresponding to the fact that the electric field now only *sees* the smaller diameter $2r_y$. The larger radius [Fig. 20(a)] leads to a redshifted resonant response of the particle, as already observed for gold circular cylinders (see Fig. 10). The same considerations hold for $k_x = 0$, as depicted in Figs. 20(c) and 20(d). Electric field maps of the periodic and isolated cases are very similar in spite of the rather small 200 nm bi-period, which further confirms the weak coupling between the elliptic nanocylinders. Above 450 nm, the subwavelength bi-periodicity selects only the specular propagation direction among all by constructive interferences.
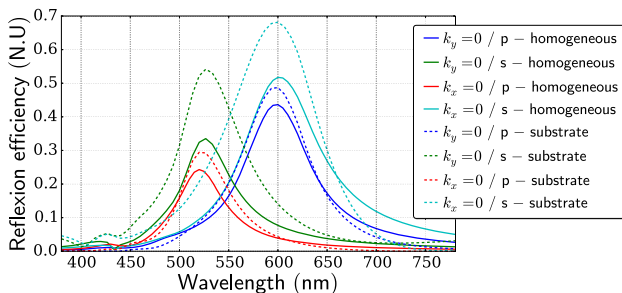

Fig. 19. (Dashed lines) Reflection efficiency in the specular order for the structure F1 (same as left panel of Fig. 12). (Solid lines) Grating of silver nanocylinders of the same dimensions as in optimized structure F1, but embedded in a homogeneous SiO_2 background. Reflection peaks in both panels are very similar.
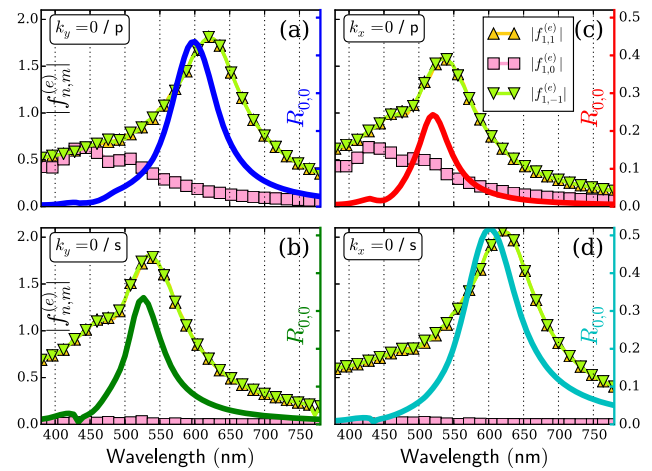

Fig. 20. Reflection of the periodic structure compared to multipolar coefficients of the isolated scatterer for incidence $\theta_0 = 29°$, with (a) $k_y = 0$ and *p* polarization, (b) $k_x = 0$ and *p* polarization, (c) $k_y = 0$ and *s* polarization, and (d) $k_x = 0$ and *s* polarization.

6. CONCLUSION

We have shown the possibility of designing efficient reflective filters with selective wavelength mirror properties together with global transparency over the visible range. A numerical tool based on the FEM has been used to analyze the behavior of nanoparticle gratings, and a comparison between numerical and experimental results has been performed. Two optimized filters with two operating wavelengths depending on the polarization have been proposed. It has been shown that Maxwell–Garnett homogenization can be used to model the considered structures. Also, the calculation of the radiation by a single nanoparticle has shown that the diffractive properties of the considered systems are governed by a single isolated particle.

Whereas the main principle has been demonstrated, the full structure can be improved in several ways to increase reflectivity and transmission. Especially, fabrication can be done now without an ITO conductive layer and without a Ti attaching layer. This should significantly reduce absorption. Besides, since the diffractive properties are governed by a single isolated particle, the same properties can be obtained with periodic or aperiodic structures as long as the size and density of the nanoparticles are the same. This may also considerably ease fabrication on large surfaces.

These promising results pave the way for smart windows and could find some innovative applications in the transport industry such as in the automotive or aeronautic sectors for displays, human–machine interfaces, and sensors.

APPENDIX A

1. Depolarization Dyadic for Circular Cylinders

The calculation of depolarization dyadic components associated with a finite circular cylinder is recalled. Let *V* be the volume of a cylinder of height *2h* and radius *R*, and let $\boldsymbol{r}$ be the vector of coordinates (x, y, z) with the origin $\boldsymbol{r} = 0$ at the center of the cylinder. Then, the dimensionless depolarization dyadic at the center of the cylinder is formally given by

$$L = - \int_V d\mathbf{r} \nabla \nabla \frac{1}{4\pi |\mathbf{r}|}. \tag{A1}$$

This expression has to be considered carefully since a singularity is present at the origin. This difficulty is fixed by splitting the integral above into a first integral over a small sphere B_0 and a second integral over the remaining volume $V \backslash B_0$. Next, using an integral over B_0 as just $1/3$ of the unit dyadic U, we have

$$L = \frac{1}{3} U - \int_{V \backslash B_0} d\mathbf{r} \nabla \nabla \frac{1}{4\pi |\mathbf{r}|}. \tag{A2}$$

Now, the Green–Ostrogradski theorem can be applied. Let S and S_0 be the surfaces of the cylinder V and the sphere B_0, respectively. The expression above becomes

$$L = \frac{1}{3} U - \int_S d s \mathbf{n} \nabla \frac{1}{4\pi |\mathbf{r}|} + \int_{S_0} d s \mathbf{n} \nabla \frac{1}{4\pi |\mathbf{r}|}. \tag{A3}$$

where ds is the infinitesimal surface element, and $\mathbf{n}$ is the outgoing normal of the surfaces. Since the last term is just $U/3$, the expression reduces to

$$L = - \int_S d s \mathbf{n} \nabla \frac{1}{4\pi |\mathbf{r}|} = \int_S d s \mathbf{n} \frac{\mathbf{r}}{4\pi |\mathbf{r}|^3}. \tag{A4}$$

Finally, using the symmetries of the cylinder, it is found that the component $L_z \equiv L_{zz}$ of the dyadic is given by the integration over the two horizontal disks at the top and bottom of the cylinder

$$L_z = 2 \int_0^R dr \int_0^{2\pi} r d\phi \frac{h}{4\pi(h^2 + r^2)^{3/2}} = 1 - \cos \theta. \tag{A5}$$

As to the components $L_x \equiv L_{xx}$ and $L_y \equiv L_{yy}$ ($L_y = L_x$ by symmetry), they are provided by integration over the vertical face of the cylinder

$$L_x = \int_{-h}^{h} dz \int_0^{2\pi} R d\phi \frac{R \cos^2 \phi}{4\pi(z^2 + R^2)^{3/2}} = \frac{1}{2} \cos \theta. \tag{A6}$$

Hence the well-known expressions [22,23] have been retrieved.

2. Depolarization Dyadic for Elliptic Cylinders

In this subsection, V and S are the volume and the surface, respectively, of a cylinder with elliptic cross section of height $2h$ and radii R_x and R_y. All the procedures performed in the circular case remain correct until Eq. (A.4). Similar to the previous case, using the symmetries of the elliptic cylinder, it is found that the component L_z is given by integration over the two horizontal surfaces S_e defined by

$$S_e = \{(x,y) | x^2/R_x^2 + y^2/R_y^2 \le 1\}. \tag{A7}$$

Then, the depolarization component in the z direction is

$$L_z = 2 \int_{S_e} dx dy \frac{h}{4\pi(h^2 + x^2 + y^2)^{3/2}}, \tag{A8}$$

which requires numerical integration to determine its value. Again using the symmetries of the cylinder, it is deduced that the depolarization factors L_x and L_y are provided by integration over the vertical face of the cylinder. The vector $\mathbf{r}$ describing this surface is (the third component z can be omitted)

$$\mathbf{r} = \begin{pmatrix} R_x \cos \phi \\ R_y \sin \phi \end{pmatrix} \Rightarrow \frac{d\mathbf{r}}{d\phi} = \begin{pmatrix} -R_x \sin \phi \\ R_y \cos \phi \end{pmatrix}, \tag{A9}$$

and the unit normal $\mathbf{n}$, orthogonal to $d\mathbf{r}/d\phi$, is then

$$\mathbf{n} = \frac{1}{\sqrt{R_x^2 \sin^2 \phi + R_y^2 \cos^2 \phi}} \begin{pmatrix} R_y \cos \phi \\ R_x \sin \phi \end{pmatrix}. \tag{A10}$$

Then, the tensor product of the two vectors $\mathbf{n}$ and $\mathbf{r}$ is given by

$$\mathbf{nr} = \frac{1}{\sqrt{R_x^2 \sin^2 \phi + R_y^2 \cos^2 \phi}}$$
$$\times \begin{pmatrix} R_x R_y \cos^2 \phi & R_x^2 \cos \phi \sin \phi \\ R_y^2 \cos \phi \sin \phi & R_x R_y \sin^2 \phi \end{pmatrix}. \tag{A11}$$

Finally, since $ds = dz d\phi \times |d\mathbf{r}/d\phi|$, the obtained expressions for the depolarization are:

$$L_x = \int_{-h}^{h} dz \int_0^{2\pi} d\phi \frac{R_x R_y \cos^2 \phi}{4\pi(z^2 + R_x^2 \cos^2 \phi + R_y^2 \sin^2 \phi)^{3/2}},$$
$$L_y = \int_{-h}^{h} dz \int_0^{2\pi} d\phi \frac{R_x R_y \sin^2 \phi}{4\pi(z^2 + R_x^2 \cos^2 \phi + R_y^2 \sin^2 \phi)^{3/2}}. \tag{A12}$$

Numerical integration is required to obtain the values of these components.

3. Depolarization Dyadic for Circular Cylinders on a Substrate

The case of a circular cylinder lying on a substrate is considered. The notations are the same as in Appendix A.1, with origin $\mathbf{r} = 0$ at the center of the cylinder of height $2h$. In addition, a substrate of relative permittivity ϵ^- is located in the half space $z < -h$ with its plane interface at the bottom circular face of the cylinder. Let $\epsilon(\mathbf{r})$ be the relative permittivity defining the environment of the cylinder: $\epsilon(\mathbf{r}) = 1$ if $z > -h$, and $\epsilon(\mathbf{r}) = \epsilon^-$ if $z < -h$. The electrostatic potential $\Phi(\mathbf{r})$ created by a point source is the solution of

$$\nabla \cdot \epsilon(\mathbf{r}) \nabla \Phi(\mathbf{r}) = \delta(\mathbf{r}). \tag{A13}$$

Denoting $\mathbf{r}_0 = 2h\mathbf{e}_z$, the solution of the equation above is

$$z > -h : \Phi(\mathbf{r}) = -\frac{1}{4\pi |\mathbf{r}|} - \frac{1 - \epsilon^-}{1 + \epsilon^-} \frac{1}{4\pi |\mathbf{r} + \mathbf{r}_0|},$$
$$z < -h : \Phi(\mathbf{r}) = -\frac{2}{1 + \epsilon^-} \frac{1}{4\pi |\mathbf{r}|}. \tag{A14}$$

The depolarization dyadic is then given by an expression equivalent to Eq. (14)

$$L = - \int_S d s \mathbf{n} \nabla \Phi(\mathbf{r}). \tag{A15}$$

Next, the calculation is similar to the one in Appendix A.1, with an additional term corresponding to the reflection part of $\Phi(\mathbf{r})$. The resulting expression for the vertical component of the depolarization dyadic is

$$L_z = 1 - \cos \theta + \frac{1 - \epsilon^-}{1 + \epsilon^-} \frac{\cos \theta - \cos \theta_1}{2}, \tag{A16}$$

where

$$\cos\theta = \frac{h}{\sqrt{h^2 + R^2}}, \qquad \cos\theta_1 = \frac{3h}{\sqrt{(3h)^2 + R^2}}. \quad \textbf{(A17)}$$

The other components of the dyadic are

$$L_x = L_y = \frac{\cos\theta}{2} - \frac{1 - \epsilon^-}{1 + \epsilon^-}\frac{\cos\theta - \cos\theta_1}{4}. \quad \textbf{(A18)}$$

This calculation can be extended to cylinders with elliptic cross section by following the procedure in Appendix A.2.

REFERENCES

1. N. Perney, J. J. Baumerg, M. E. Zoorob, M. D. Charlton, S. Mahnkopf, and C. M. Netti, "Tuning localized plasmons in nanostructured substrates for surface-enhanced Raman scattering," Opt. Express **14**, 847–857 (2006).
2. J. N. Yih, Y. M. Chu, Y. C. Mao, W. H. Wang, F. C. Chien, C. Y. Lin, K. L. Lee, P. K. Wei, and S. J. Chen, "Optical waveguide biosensors constructed with subwavelength gratings," Appl. Opt. **45**, 1938–1942 (2006).
3. K. Kumar, H. Duan, R. S. Hegde, S. C. W. Koh, J. N. Wei, and J. K. W. Yang, "Printing colour at the optical diffraction limit," Nat. Nanotechnol. **7**, 557–561 (2012).
4. G. Si, Y. Zhao, J. Lv, M. Lu, F. Wang, H. Liu, N. Xiang, T. J. Huang, A. J. Danner, J. Teng, and Y. J. Liu, "Reflective plasmonic color filters based on lithographically patterned silver nanorod arrays," Nanoscale **5**, 6243–6248 (2013).
5. C. W. Hsu, B. Zhen, W. Qiu, O. Shapira, B. G. DeLacy, J. D. Joannopoulos, and M. Soljačić, "Transparent displays enabled by resonant nanoparticle scattering," Nat. Commun. **5**, 3152 (2014).
6. T. Xu, Y.-K. Wu, X. Luo, and L. J. Guo, "Plasmonic nanoresonators for high-resolution colour filtering and spectral imaging," Nat. Commun. **1**, 59 (2010).
7. B. Zeng, Y. Gao, and F. J. Bartoli, "Ultrathin nanostructured metals for highly transmissive plasmonic subtractive color filters," Sci. Rep. **3**, 2840 (2013).
8. G. Demésy, F. Zolla, A. Nicolet, and M. Commandré, "All-purpose finite element formulation for arbitrarily shaped crossed-gratings embedded in a multilayered stack," J. Opt. Soc. Am. A **27**, 878–883 (2010).
9. L. Li, "Fourier modal method," in *Gratings: Theory and Numeric Applications*, 2nd revisited ed., E. Popov, ed. (Aix-Marseille Université, CNRS, Centrale Marseille, Institut Fresnel, 2014), Chap. 13.
10. M. J. Weber, *Handbook of Optical Materials*, vol. **19** (CRC Press, 2002).
11. P. B. Johnson and R. W. Christy, "Optical constants of the noble metals," Phys. Rev. B **6**, 4370–4379 (1972).
12. E. D. Palik, *Handbook of Optical Constants of Solids* (Academic, 1998), Vol. **3**.
13. A. D. Rakić, A. B. Djiurisic, J. M. Elazar, and M. L. Majewski, "Optical properties of metallic films for vertical-cavity optoelectronic devices," Appl. Opt. **37**, 5271–5283 (1998).
14. A. Nicolet, S. Guenneau, C. Guezaine, and F. Zolla, "Modelling of electromagnetic waves in periodic media with finite elements," J. Comput. Appl. Math. **168**, 321–329 (2004).
15. J.-P. Berenger, "A perfectly matched layer for the absorption of electromagnetic waves," J. Comput. Phys. **114**, 185–200 (1994).
16. C. Geuzaine and J.-F. Remacle, "Gmsh: A 3-D finite element mesh generator with built-in pre- and post-processing facilities," Int. J. Numer. Methods Eng. **79**, 1309–1331 (2009).
17. P. Dular, C. Guezaine, F. Henrotte, and W. Legros, "A general environment for the treatment of discrete problems and its application to the finite element method," IEEE Trans. Magn. **34**, 3395–3398 (1998).
18. N. A. Nicorovici and R. C. McPhedran, "Transport properties of arrays of elliptical cylinders," Phys. Rev. E **54**, 1945–1957 (1996).
19. V. Mityushev, "Conductivity of a two-dimensional composite containing elliptical inclusions," Proc. R. Soc. A **465**, 2991–3010 (2009).
20. B. Stout, M. Nevière, and E. Popov, "Mie scattering by an anisotropic object. Part i: Homogeneous sphere," J. Opt. Soc. Am. A **23**, 1111–1123 (2006).
21. B. Stout, M. Nevière, and E. Popov, "Mie scattering by an anisotropic object. Part ii: Arbitrary-shaped object: differential theory," J. Opt. Soc. Am. A **23**, 1124–1134 (2006).
22. A. D. Yaghjian, "Electric dyadic green's functions in the source region," Proc. IEEE **68**, 248–263 (1980).
23. J. G. Van Bladel, *Electromagnetic Fields* (Wiley, 2007).